IOP Publishing Journal of Physics: Condensed Matter
J. Phys.: Condens. Matter **32** (2020) 205702 (9pp) https://doi.org/10.1088/1361-648X/ab6f84

The superconductivity and topological surface state of type-II Dirac semimetal $NiTe_2$

Jie Zhang and G Q Huang

Department of Physics, Nanjing Normal University, Nanjing 210023, People's Republic of China

E-mail: huangguiqin@njnu.edu.cn

Received 7 October 2019, revised 8 January 2020
Accepted for publication 24 January 2020
Published 20 February 2020

Abstract

$NiTe_2$ is a type-II Dirac semimetal with the Dirac point very close to the Fermi level. In this paper, its electronic structure, phonon structure and electron–phonon interaction are studied via first-principles calculations. The noteworthy result is that the nontrival bands around the type-II Dirac point are strongly coupled with phonon modes, suggesting that they play an important role in superconductivity. Furthermore, the topological surface states on the (0 0 1) cleavage plane originated from the nontrivial Z_2 are well separated from the bulk states and can be tuned to approach the Fermi level by adding holes or by V substitution. The possible topological superconductivity in type-II Dirac semimetal $NiTe_2$ is discussed.

Keywords: type-II Dirac semimetal, topological surface state, superconductivity, electron–phonon coupling

(Some figures may appear in colour only in the online journal)

1. Introduction

Dirac and Weyl semimetal (WSM) are two kinds of topological materials [1–4]. In Dirac semimetal (DSM), the linear band crossing is fourfold degenerated point (so-called Dirac point). By breaking inversion symmetry or time-reversal symmetry, a Dirac cone can split into a pair of Weyl cones and form WSM. DSM and WSM have two types. For a conventional type-I semimetal, such as Cd_3As_2 [5] and TaAs [6], the Fermi surface is point-like. When the cone of the linear dispersion relation is tilted beyond a critical angle, highly anisotropic type-II DSM or WSM is formed [7]. For the latter case, the Lorentz invariance is broken and the Fermi surface contains both electron and hole pockets near the Dirac or Weyl points. Some materials, such as WTe_2 [7], $MoTe_2$ [8], $Mo_xW_{1-x}Te_2$ [9] and TMX_2 (TM = Ni, Pd, Pt; X = Se, Te) family [10–17] are found to be type-II semimetals. Type-II semimetals may appear a number of new physical phenomena, such as an angle-dependent chiral anomaly and topological Lifshitz transitions [18].

Due to the intrinsic topology of DSMs or WSMs, topological superconductivity may be achieved from them. Topological superconductors attract much attention because they are predicted to host protected Majorana zero modes (for some reviews, see [19, 20]) with possible applications in topological quantum computation [21] and in some functional devices such as topological strain effect transistor [22]. A great deal of interest both experimentally and theoretically has been triggered to reveal the interplay of superconductivity and topology in DSMs or WSMs [7, 13, 22–29]. For a superconducting WSM, it is shown that both intranodal finite momentum pairing and internodal BCS superconductivity are allowed to display robust odd-parity superconductivity [27]. However, for robustly protected surface Fermi arcs in an inversion-symmetric WSM, they remain gapless even in the superconducting states since there is no partner electron to form a Cooper pair [19]. For a superconducting DSM, it can show unique pairing symmetries. Due to the presence of time-reversal symmetry and inversion symmetry in DSM, the electronic excitation near the Dirac point is described by a four-component Dirac fermion with spin and orbital degrees of freedom, which exhibits nontrivial orbit-momentum locking [28, 29]. It is found that orbit-momentum locking critically affects the possible pairing symmetry in the superconducting

states. When the interorbital attraction is sufficiently stronger than the intraorbital one, an unconventional odd-parity pairing state with point nodes appear [28, 29]. The unconventional superconducting states show either dispersive or flat Andreev bound states on the surface depending on the parity of mirror reflection symmetry [28].

The superconductivity in type-II semimetals has received more attention due to a finite density of states around the crossing point. The tilt of the Dirac or Weyl cone can render semimetal to a type-II phase. As recently demonstrated, control of tilting parameter can be realized, for example, by applying strain [22, 25, 26, 30], pressure [23], or doping [24]. Experimental studies have observed enhancements in the critical temperature of superconducting $MoTe_2$ under pressure [23], by applying mechanical strain [26], or through partially substituting the tellurium ions by sulfur [24]. This enhancement might be due to the topological transition from type-I to type-II WSM phase as recently explored in theory [31, 32].

Recently, type-II DSMs [10–17] are predicted to be realized in TMX_2 (TM = Ni, Pd, Pt; X = Se, Te) compounds and confirmed by experiments, in which there is a Dirac cone titled along the [0 0 1] direction. The Dirac point is located below the Fermi level (E_F) with a binding energy of 0.8 eV in $PtTe_2$, 1.2 eV in $PtSe_2$, and 0.6 eV in $PdTe_2$ [10–12]. However, for $NiTe_2$ material [17], this type-II Dirac point is located very close to the E_F. The quantum oscillations in this material reveal a nontrivial Berry's phase associated with this Dirac fermion. The first-principles calculations about $NiTe_2$ compound [17] show that the Dirac points located at $\mathbf{k} = (0, 0, \pm 0.35)(2\pi/c)$ are very close to E_F compared with other materials in this series [10–12, 15].

For TMX_2 (TM = Ni, Pd, Pt; X = Se, Te) type-II DSMs, there are many experimental studies of superconductivity in them. Superconductivity is found in $PdTe_2$ with $T_c \sim 1.78$ K [2, 33, 34], and can be enhanced in its Cu intercalated form $Cu_{0.05}PdTe_2$ with $T_c = 2.4$ K [35] and in the Au substitution form with $T_c = 4.65$ K [36]. Through direct measurement of the superconducting energy gap by scanning tunneling spectroscopy [37], the results show that the superconductivity in $PdTe_2$ is conventional. Heat capacity measurements also show that the superconductivity in $PdTe_2$ is conventional in nature [38]. However, magnetic and transport measurements [39] show that $PdTe_2$ is a 'kind-I' superconductor, which is generally unexpected for binary compounds. Leng *et al* [40] also reveal that superconductivity maintains its 'kind-I' character under pressure. The first-principles calculations [2] reveal that the superconductivity of $PdTe_2$ originates mainly from the electrons at the van Hove singularity (vHs) band near E_F, but not the type-II Dirac bands below E_F. For the isostructural $NiTe_2$ compound, Lima *et al* [41] investigate the effect of Ti doping and they find that this compound shows superconductivity with the superconductivity temperature reached 4.0 K. But the application of pressure up to 1.3 GPa has no effect on the superconducting states. It is also suggested that the superconductivity may be induced in the $NiTe_2$ upon Cu intercalation [42]. Owing to the type-II Dirac nodes in $NiTe_2$ are much closer to the E_F compared with other compounds in this series, it may be a good candidate to become topological superconductor. To better understand the superconductivity of $NiTe_2$ material, detailed theoretical calculation is highly desirable. This is one motivation of this study.

Surface superconductivity in $PdTe_2$ has also been observed experimentally. Point-contact spectroscopy study [43] shows a single full gap with mixed 'kind-I' and 'kind-II' superconductivity on surface of the type-II DSM $PdTe_2$. Magnetic and transport measurements [39] show that surface superconductivity below 1.33 K is at odds with the standard BCS behavior. When pressure exceeds 1.41 GPa [40], the superconducting transition temperature for the surface is larger than that of the bulk, showing that surface and bulk superconductivity have distinct phenomena. Leng *et al* [40] propose that surface superconductivity possibly has a nontrivial nature and originates from topological nontrivial surface states. The Dirac point of the (0 0 1) surface states originating from a nontrivial Z_2 invariant has been found in $PdTe_2$, $PtSe_2$ and $PtTe_2$ compounds by angle-resolved photoemission measurements or by theoretical calculations [10–12, 14, 44, 45]. It looks like a typical Dirac cone in a TI (topological insulator) [46, 47]. However, this nontrivial surface state lies deeply below the E_F. The calculations for $NiTe_2$ compound [17] indicate that this topological surface state lies about 1.6 eV below the E_F. These topological surface states, however, are too far below the E_F to play any role in the superconductivity of this kind of system. To search for two-dimensional (2D) topological superconductivity in $NiTe_2$ and related compounds, it is necessary to tune the binding energy of the Dirac point to E_F while retaining the superconductivity. This is another motivation of this study.

In this work, electronic structure, phonon structure and electron–phonon (EP) interaction of $NiTe_2$ are systematically studied via first-principles calculations. The noteworthy result is that both the vHs band and the nontrival bands around type-II Dirac point are strongly coupled with phonon modes, suggesting that they play an important role in superconductivity. The nontrivial topological surface state on (0 0 1) cleavage plane in $NiTe_2$ is calculated and it can be tuned to approach the E_F by adding two holes or by V substitution. Finally, we discuss the possible topological superconductivity both in the bulk and on the surface.

2. Computational method

We will perform first-principles simulation calculations through the PWSCF program of the Quantum-ESPRESSO distribution [48] based on the density functional theory. Norm-Conserving ONCVPSP pseudopotential [49] and general gradient approximation for the exchange and correlation energy are used. Kinetic energy cutoff in the plane-wave basis set is 80 Ry. Electronic and vibrational states are computed by sampling the Brillouin zone (BZ) on a (12,12,8) and (6,6,4) Monkhorst–Pack grids, respectively. To probe the surface structure, a first-principles tight-binding (TB) model Hamilton is constructed, which are calculated by projecting onto the Wannier orbital through the WANNIER90 program [50]. We use the Ni-*d* orbital and Te-*s* orbital as well as Te-*p*

orbital for the initial projection. The surface state spectrum of $NiTe_2$ on (0 0 1) surface is calculated with the surface Greens function methods as implemented in WannierTools [51]. EPW program is used to calculate the EP interaction [52].

3. Results and discussion

3.1. Superconductivity

$NiTe_2$ crystallizes in the CdI_2-type hexagonal structure with $P\bar{3}m1$ space group [2], as shown in figure 1(a). The corresponding BZ is shown in figure 1(b). Stable geometric structure of $NiTe_2$ at ambient conditions is 1T phase [53], i.e. stacking of the atomic planes is an */ABC/* sequence along z axis. Ni and Te consist of stacked Te–Ni–Te layers, where the metal Ni atom is coordinated octahedrally with six Te atoms. The atoms are covalently bonded within one layer, while the sandwich layers are coupled only by weak van der Waals interaction [36]. So (0 0 1) surface of $NiTe_2$ compound is its natural cleavage plane. Our optimized lattice constants are $a = b = 3.90$ Å and $c = 5.30$ Å, which are consistent very well with the experimental values ($a = b = 3.86$ Å, $c = 5.27$ Å) [17].

The calculated electronic band structures of $NiTe_2$ along some high symmetry directions without and with spin–orbit coupling (SOC) are shown in figures 1(c) and (d). The electronic structure of $NiTe_2$ shows strong three-dimensionality, as manifested from the different band structures on the Γ-M-K and L- H-A planes. When SOC is turned on, originally double degenerate bands at some high symmetry points (such as Γ, A, K, H) or along some high symmetry directions (such as $\Gamma - A$) split. There are five bands crossing the E_F without SOC. When SOC is turned on, due to large splitting between b_2 and b_3 bands ($\Delta E = 0.8$ eV as shown in figure 1(d)), b_3 band falls below the E_F and correspondly there are eight bands crossing the E_F (i.e. fours bands with Kramers degeneracy). A saddle-point vHs is observed just at E_F near the high symmetry point M. This vHs band can also be found in $PdTe_2$ and $PtTe_2$ compounds [2]. The obtained density of states (DOS) shown at the right panels in figures 1(c) and (d) are very similar, in which the E_F locates almost at the valley of the DOS curve. In the following, we mainly focus on the calculated results with SOC. The projected DOS can be seen in figure 1(d). The primary contribution near the E_F is mainly from Te-p orbital electrons, while Ni-d orbital electrons contribute mainly in the range from -5 eV to -1 eV below the E_F. There is slight hybridization between Ni-d and Te-p near the E_F. 2D top view and three-dimensional view of Fermi surface with SOC are shown in figures 1(e) and (f). Multi-band crossing with E_F leads to the complex Fermi surface. The Fermi surface consists of a twisted triangular prism shaped hole pocket in the BZ center, a lantern shaped together with six dot shaped hole pockets, a gear shaped electron pocket around the boundary of $k_z = 0$ plane, and six small electron pockets at the K points.

Our calculations indicate the existence of type-II Dirac point in $NiTe_2$, which is the crossing point between b_1 and b_2 bands and is shown by 'D' in figures 1(c) and (d). When SOC is taken into consideration, the pair of Dirac points are located at $\mathbf{k} = (0, 0, \pm 0.35)(2\pi/c)$ along the $\Gamma - A$ direction, which is consistent with previous study [17]. It is about 0.2 eV (0.1 eV) below (above) E_F without SOC (with SOC). The Dirac point in $NiTe_2$ is much closer to E_F compared with 0.8 eV below the E_F in $PtTe_2$ and 0.6 eV below the E_F in $PdTe_2$ [10–12], implying that $NiTe_2$ may be a good candidate to realize topological superconductor. $NiTe_2$ belongs to the type-II DSM. The Hamiltonian of Dirac cone in three-dimensional systems is given by [54]:

$$H = \boldsymbol{\omega} \cdot \mathbf{k}\hat{I} + \sum_{\mu=x,y,z} v_\mu k_\mu \hat{\sigma}_\mu. \quad (1)$$

Here, $\boldsymbol{\omega}$ is related to the tilt from the z axis, $\hat{I}$ is the unit matrix, $\mathbf{k}$ is momentum (take $\hbar = 1$), $\hat{\sigma}$ is the Pauli matrice, v_μ is anisotropic Fermi velocity. As to $NiTe_2$, the Dirac cone is only tilted along k_z direction, $\omega_z > v_z$ forms a type-II Dirac cone. The Dirac cone of $NiTe_2$ is shown in figures 1(g) and (h), it is untilted on k_x–k_y plane but tilted strongly on k_x–k_z plane, presenting the typical character of type-II DSM [10].

The phonon structure is calculated from the density functional perturbation theory [48]. The calculated phonon dispersions of $NiTe_2$ along major high symmetry lines are shown in figure 2(a). We can see that there is no imaginary frequency in the full phonon spectra, indicating its dynamical stability. There are three atoms in the unit cell, which gives rise to nine phonon modes. According to the group theory classification, the Γ-point modes can be decomposed as $2E_u \oplus 2A_{2u} \oplus E_g \oplus A_{1g}$. Here all the A modes are vibrations along the z axis, and all the E modes are doubly degenerate in-plane vibrations. Among them, E_u and A_{2u} are infrared active, while E_g and A_{1g} are Raman active. Atomic displacements of the two Raman active modes are plotted in figure 2(b). E_g and A_{1g} are the so-called homopolar modes, where Te atoms vibrate in counter-phase while the Ni atom remains stationary. Our calculated frequencies are 2.4 THz (80.4 cm^{-1}) and 4.1 THz (135.7 cm^{-1}) for E_g and A_{1g} Raman active modes, respectively. Our obtained frequency value is in good agreement with that of Raman spectroscopy [17], which gives 76 cm^{-1} for E_g Raman mode. Furthermore, our obtained Debye temperature ($\Theta_D = 234$ K) of $NiTe_2$ compound is also very close to the experimental value ($\Theta_D = 230$ K) [17]. The calculated total and the projected phonon DOS for the single atom are shown in figure 2(c). There is a gap from 4.1 THz to 5.3 THz. The acoustic modes and the so-called homopolar modes arisen from the vibrations of Te atoms are occupied below this gap. The Ni–Te bond-stretching modes are occupied above the gap due to the strong Ni–Te covalent bond. The states above (below) the gap are mainly from the vibrations of Ni (Te) atom due to the large difference of mass between Ni and Te atoms. Meanwhile, we find that overall features of the phonon dispersion and phonon DOS for $NiTe_2$ in figures 2(a) and (c) are essentially the same as those of $PdTe_2$ [2].

The EP interaction is estimated according to the Migdal-Eliashberg theory [55]. The approximations taken and the technical details for calculating the electron and phonon self-energies arising from the EP interaction are described in [56]. The imaginary parts of the electron ($\Gamma_{n\mathbf{k}}$) and phonon ($\Gamma_{\mathbf{q}\nu}$)

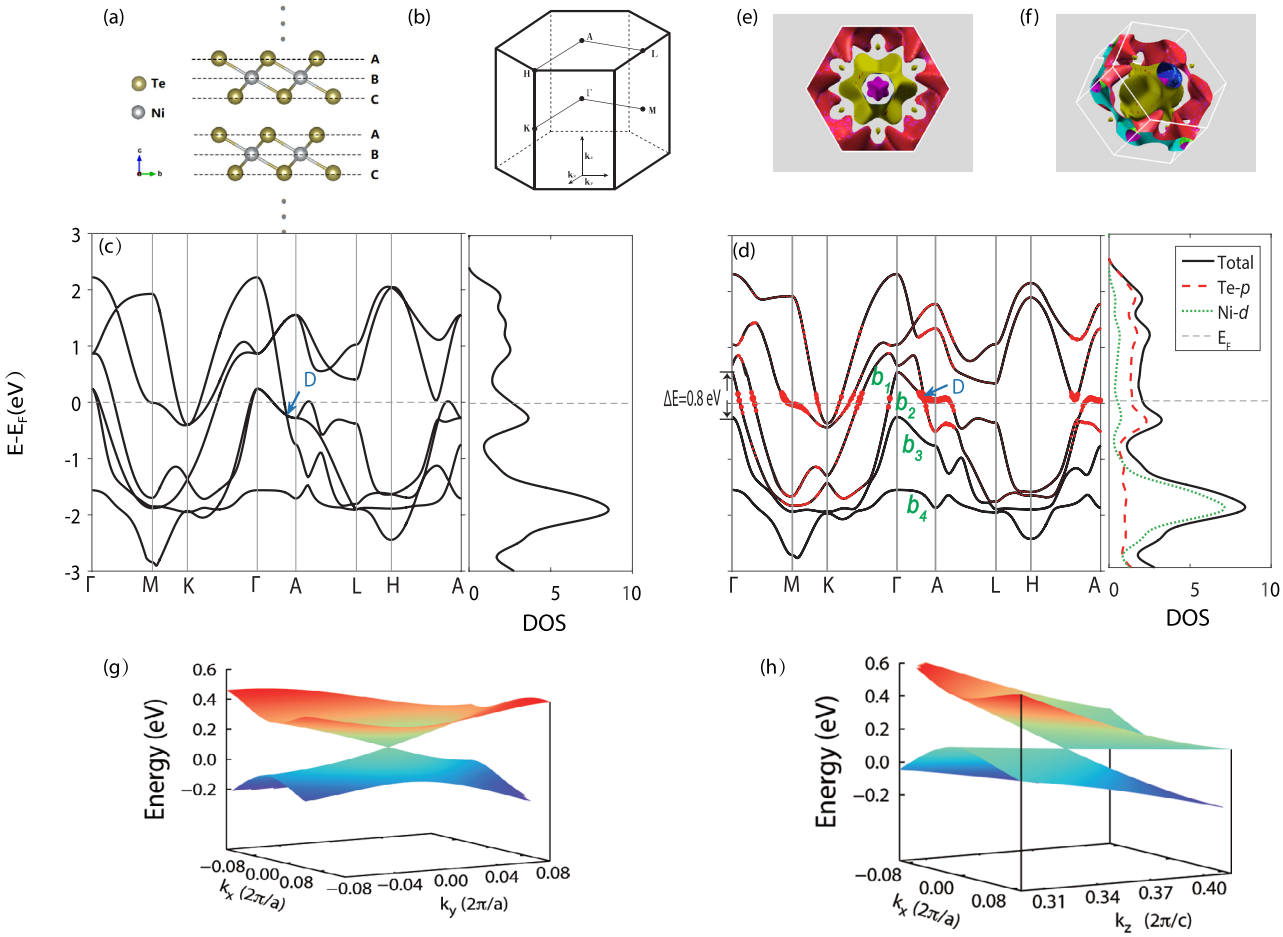

Figure 1. (a) Schematic crystal structure of $NiTe_2$ and (b)the corresponding BZ; Band structure (left panel) and DOS (rignt panel) of $NiTe_2$ without SOC (c) and with SOC, the electron linewidth induced by phonon is shown by the red dots in figure (d); (e) 2D top view and (f) three-dimensional view of Fermi surface with SOC; Type-II Dirac cone on k_x–k_y plane (g) and on k_x–k_z plane (h).

self-energies, i.e. the corresponding linewidths at the temperature T are given by [56]:

$$\Gamma_{n\mathbf{k}}(T) = \pi\Sigma_{m\nu}\int_{\mathrm{BZ}}\frac{\mathrm{d}\mathbf{q}}{\Omega_{\mathrm{BZ}}}\times|g_{mn,\nu}(\mathbf{k},\mathbf{q})|^2 \times\{[n_{\mathbf{q}\nu}(T)+f_{m\mathbf{k}+\mathbf{q}}(T)]\times\delta(\varepsilon_{n\mathbf{k}}-\varepsilon_{m\mathbf{k}+\mathbf{q}}+\omega_{\mathbf{q}\nu}) +[n_{\mathbf{q}\nu}(T)+1-f_{m\mathbf{k}+\mathbf{q}}(T)]\times\delta(\varepsilon_{n\mathbf{k}}-\varepsilon_{m\mathbf{k}+\mathbf{q}}-\omega_{\mathbf{q}\nu})\} \quad (2)$$

$$\Gamma_{\mathbf{q}\nu}(T) = 2\pi\Sigma_{mn}\int_{\mathrm{BZ}}\frac{\mathrm{d}\mathbf{k}}{\Omega_{\mathrm{BZ}}}\times|g_{mn,\nu}(\mathbf{k},\mathbf{q})|^2\times(f_{n\mathbf{k}}(T) -f_{m\mathbf{k}+\mathbf{q}}(T))\times\delta(\omega_{\mathbf{q}\nu}+\varepsilon_{n\mathbf{k}}-\varepsilon_{m\mathbf{k}+\mathbf{q}}). \quad (3)$$

Here, $g_{mn,\nu}(\mathbf{k},\mathbf{q})$ is an EP matrix element which strongly affects the Eliashberg function especially for low phonon frequencies, and can be determined self-consistently from the calculation [52]. The first and second terms in square brackets in equation (2) correspond to phonon absorption and emission, respectively, and the temperature dependence of the scattering rate stems from the electron and phonon occupation factors n and f, respectively. The factor of '2' in equation (3) accounts for the spin degeneracy. $\varepsilon_{n\mathbf{k}}$ is the energy of the electronic state $|n\mathbf{k}>$ associated with the momentum in $\mathbf{k}$ space and the energy band index n. $\omega_{\mathbf{q}\nu}$ is the phonon frequency associated with the wave vector $\mathbf{q}$ and the phonon band index ν. Ω_{BZ} is the volume of BZ. From the electron linewidth, one can identify which electronic bands are strongly coupled with phonon modes. Our calculated electron linewidth for bands near the E_{F} is shown by the red dots in figure 1(d). The size of the red dots is proportional to the size of the electron linewidth. It can be seen that vHs band near M point has large linewidth, manifesting strong EP coupling. This is very similar to that in $PdTe_2$. Kim *et al* [2] have found that the saddle-point vHs near the E_{F} plays an important role in superconducting $PdTe_2$. Furthermore, it's particularly noteworthy that the nontrival bands around type-II Dirac point are strongly coupled with phonon modes too, which indicates possibilities to realize topological superconductivity in $NiTe_2$. From the phonon linewidth, one can identify which phonon modes are strongly coupled with electron bands. The phonon linewidth of $NiTe_2$ is shown by red dots in figure 2(a). The marker size is proportional to its phonon linewidth. It is noted that the linewdith is obviously large around 2.4 THz at Γ point, which indicates in-plane E_g optical modes are strongly coupled with electron bands.

Next, we calculate the Eliashberg function $\alpha^2F(\omega)$ and the cumulative contribution to the EP coupling strength $\lambda(\omega)$,

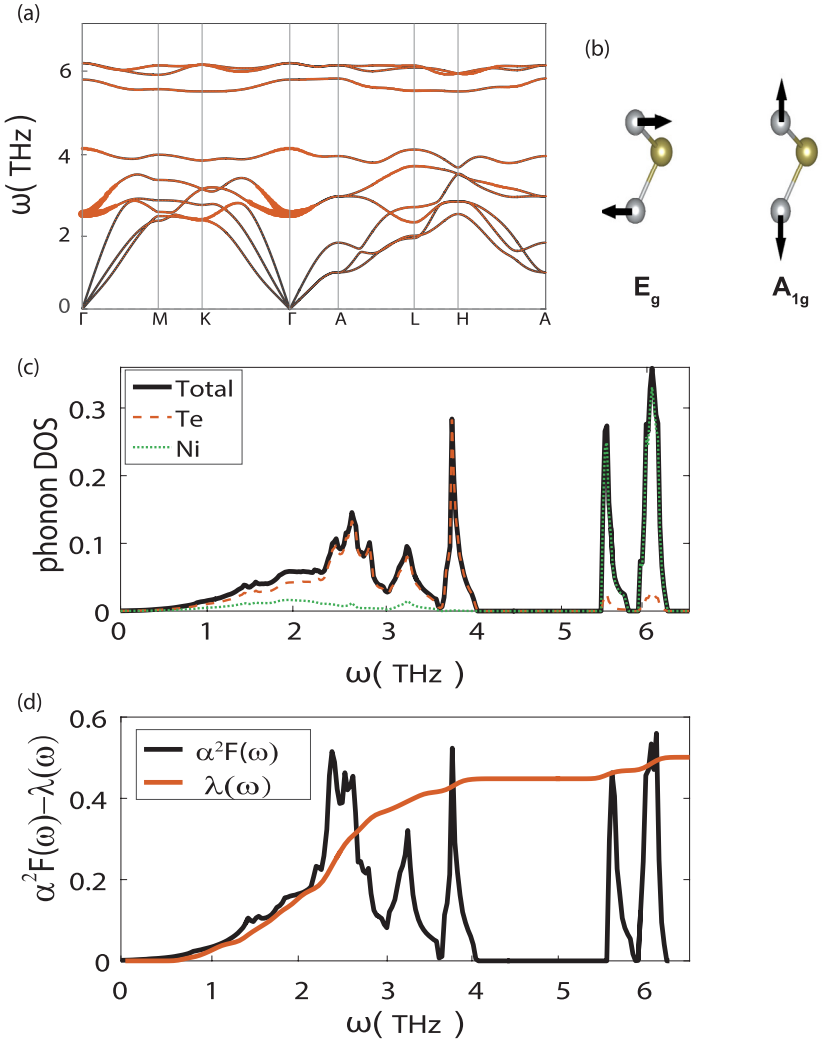

Figure 2. (a)Phonon spectrum of $NiTe_2$, the phonon linewidth is shown by the red dots ; (b) The atomic displacement of two Raman active modes; (c) Phonon DOS and the projected DOS; (d) Eliashberg function $\alpha^2F(\omega)$ and the cumulative contribution to the EP coupling strength $\lambda(\omega)$.

which are obtained from the following expressions and are shown in figure 2(d):

$$\alpha^2F(\omega) = \frac{1}{2\pi N_{E_F}} \sum_{\mathbf{q}\nu} \frac{\lambda_{\mathbf{q}\nu}}{\omega_{\mathbf{q}\nu}} \delta(\omega - \omega_{\mathbf{q}\nu}) \tag{4}$$

$$\lambda(\omega) = 2\int_0^{\omega} \frac{\alpha^2F(\omega')}{\omega'} \mathrm{d}\omega' \tag{5}$$

where N_{E_F} is the DOS at the E_F, $\lambda_{\mathbf{q}\nu}$ is the phonon wave vector $\mathbf{q}$ and mode ν resolved EP coupling constant. One can see that $\alpha^2F(\omega)$ in figure 2(d) and $F(\omega)$ in figure 2(c) are similar in shape to each other, indicating that all the vibration modes have contributions to the EP interaction. However, we can find that the peak around 2.4 THz has large contribution to the EP interaction, we get $\lambda(\omega = 3\ \mathrm{THz}) = 0.4$, being about 80% of the total EP coupling ($\lambda(\omega = \infty) = 0.51$). According to the formula of equation (5), the phonon frequency appears in the denominator, so several peaks above 3.5 THz have small contribution to the EP coupling.

Using Allen–Dynes formula to estimate T_c [57]

$$T_c = \frac{\omega_{\log}}{1.2} \exp\left(\frac{-1.04(1+\lambda)}{\lambda - \mu^*(1+0.62\lambda)}\right) \tag{6}$$

where μ^* is the coulomb repulsion parameter, $\omega_{\log}$ is the logarithmically averaged frequency and is given by

$$\omega_{\log} = \exp\left(\frac{2}{\lambda}\int \log\omega \frac{\alpha^2F(\omega)}{\omega}\right)\mathrm{d}\omega. \tag{7}$$

Our obtained value is $\omega_{\log} = 2.4$ THz. Taking $\mu^* = 0.1$, T_c is estimated to be 1.5 K within the conventional BCS theory.

It is very interesting to compare our results of $NiTe_2$ to that of $PdTe_2$. Both of them have saddle-point vHs band near the E_F, which plays an important role in superconductivity. Although both of them belong to type-II DSM, however, the locations of Dirac points are different. In $PdTe_2$, the Dirac point is located about 0.6 eV below the E_F, which is too far from the E_F to participate in the superconductivity. The experiments show that the superconducting phase in $PdTe_2$ is conventional in nature [37, 38]. In $NiTe_2$, the Dirac point is located very near the E_F and our calculations also show that the nontrival bands around type-II Dirac point are strongly coupled with phonon modes,

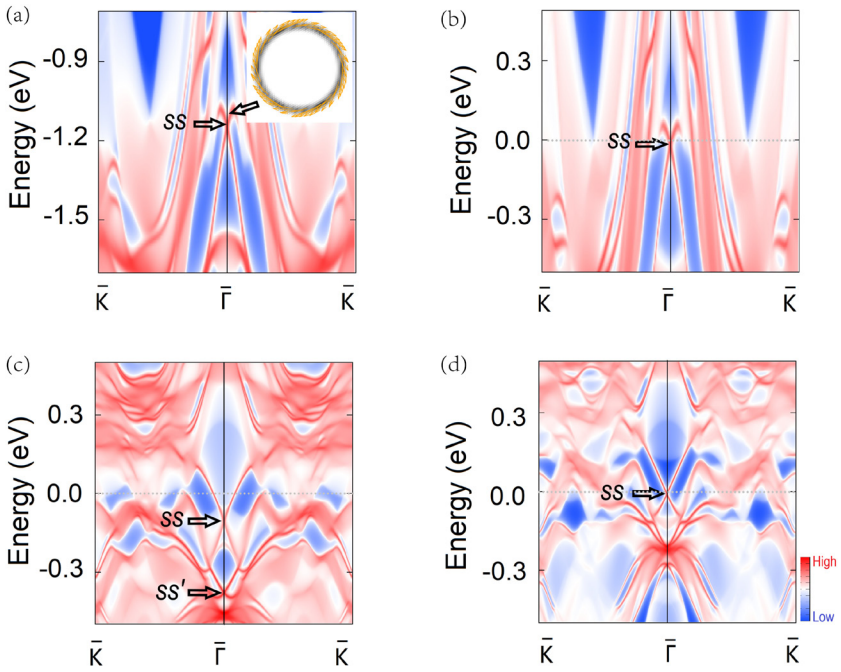

Figure 3. Projected surface density of states for the (0 0 1) surface of $NiTe_2$ (a), two holes-doped $NiTe_2$ (b), Cr-doped $NiTe_2$ (c) and V-doped $NiTe_2$ (d).

suggesting the possibility to realize topological superconductivity in $NiTe_2$.

3.2. Topologically nontrivial surface state

The presence of a topologically nontrivial surface state is another striking feature in type-II DSM $NiTe_2$ [17]. We calculate the surface states on (0 0 1) cleavage on the TB hamiltonian from projected Wannier functions. The projected surface states along $\overline{K}-\overline{\Gamma}-\overline{K}$ direction is shown in figure 3(a). The projected type-II Dirac point is hidden in the continuous bulk states. However, there exists a Dirac topological surface state (shown by 'SS' in figure 3(a)) lying about 1.2 eV below the E_F due to the nontrivial Z_2 topological gap (between b_3 and b_4 bands as marked in figure 1(d)). The calculation by Xu *et al* [17] gives the position of this surface state located at about 1.6 eV below the E_F. This difference may be due to the different pseudopotential used between our calculation and [17]. $NiTe_2$ compound has inversion-symmetry, its topology can be described by one strong topological index ν_0 and three weak indices ν_1,ν_2,ν_3 [31]. Our calculated four topological indices $\nu_0;(\nu_1,\nu_2,\nu_3)$ is 0;(0,0,1), implying a weak topological property in $NiTe_2$. The dispersion of this surface bands around $\overline{\Gamma}$ point is linear and is well separated from the bulk states. In order to understand the spin pattern in momentum space, the spin expectation values are calculated through the package available within Quantum-ESPRESSO [48]. The calculated spin-polarization component is shown in the inset in figure 3(a). The spin orientation is locked in-plane and perpendicular to the electron momentum **k**. The spin-polarization rotates around the $\overline{\Gamma}$ point, which looks like a typical Dirac cone in a TI [58]. However, the surface state is too far below the E_F, so it is necessary to adjust this Dirac point to E_F while the material retains the superconductivity. It is a common way to dope holes to tune the E_F down to this Dirac point. Theoretical assumption and element substitution are employed to realize hole doping in the following study.

For the scheme of the theoretical assumption, two holes are added. Meantime a compensating jellium background is inserted to remove divergences if the cell is not neutral in a periodic calculation [48]. Experimentally, electron or hole doping can be realized by gate electrode and the amount of doping can also be varied by simply changing the gate voltage using gated device [59]. After doping with two holes, we find that there is no noticeable change in electronic structure except for the downshift of the E_F (i.e. rigid band model). Our obtained surface states are shown in figure 3 (b). It can be clearly seen that this Dirac topological surface state due to the nontrivial Z_2 topology is now located near the E_F.

Another scheme of hole doping is employed by element substitution. We construct a 2×2 supercell with 12 atoms and one of Ni atoms is substituted with V or Cr, which corresponds to doping concentration of 25%. The band structures of them are shown in figure 4. For the calculation without SOC, the type-II Dirac point (around 0.18 eV above the E_F) still exist for Cr doping as shown by 'D' in figure 4(a), but it disappears when substituting with V atom (see figure 4(c)). However, when taking SOC into consideration, it is interesting to find that b_1 and b_2 bands intersect twice along $\overline{\Gamma}-\overline{A}$ direction for both Cr and V doping and there emerge two closely located type-II Dirac points as shown by 'D_1' and 'D_2' in figures 4(b) and (d). The projected surface states for Cr and V doping are shown in figures 3(c) and (d). For Cr substitution, a Dirac cone-like surface state(shown by '*SS*') is merged into continuous bulk states. But for V substitution, an apparent Dirac cone-like surface state ('*SS*') occurs very closely to the E_F. Its dispersion

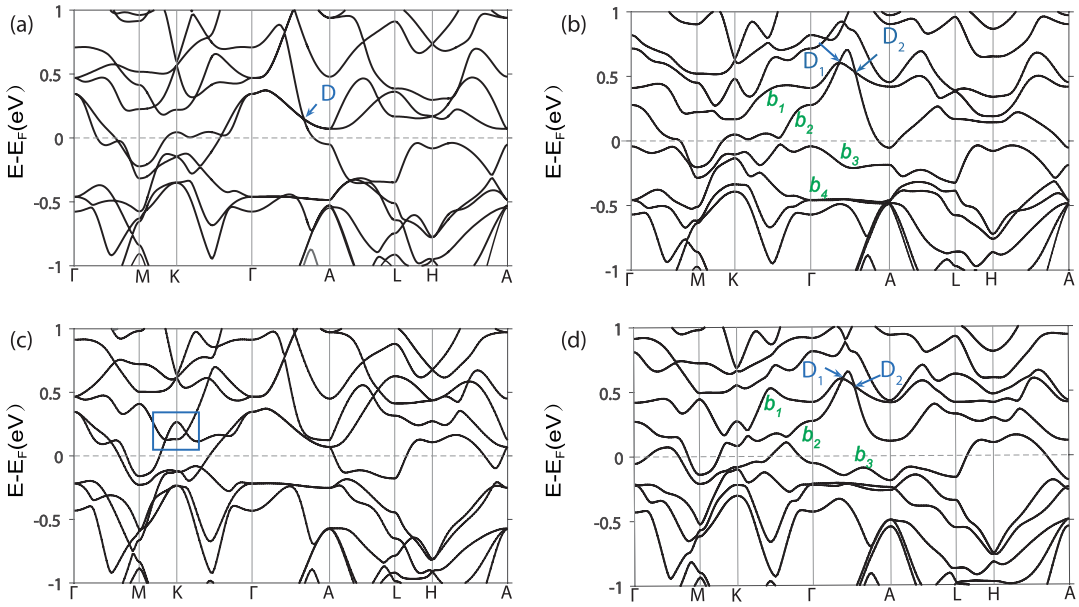

Figure 4. Band structure of Cr-doped $NiTe_2$ (a)/(b) and V-doped $NiTe_2$ (c)/(d) without/(with) SOC.

is linear and is well separated from the bulk states. Our study shows that surface state ('*SS*') is due to the nontrivial Z_2 topological gap (between b_2 and b_3 bands as marked in figure 4). Our calculated four topological indices $\nu_0;(\nu_1,\nu_2,\nu_3)$ are 1;(0,0,1) and 0;(0,0,1), which implies a strong topological property and a weak topological property for Cr and V doping, respectively. The different topology between Cr and V doping can be understood by analyzing their band structures from figure 4. In figure 4(c) for V substitution, there is a band inversion at K point (sketched by the blue rectangle), resulting in a nodal ring in the $k_z = 0$ plane, while this band inversion is absent in figure 4(a) for Cr substitution. The different band sequence in the $k_z = 0$ plane and the same band sequence in the $k_z = \pi/c$ plane result in different topological property for Cr and V substitution. Furthermore, for Cr substitution, we notice that there is another Dirac cone-like surface state ('*SS*′') separated from the bulk states as shown in figure 3(c) due to the nontrivial Z_2 topological gap between b_3 and b_4 bands, but it is slightly far from the E_F.

According to our calculations, the nontrivial topological surface state in $NiTe_2$ can be tuned to near the E_F by adding two holes or by V substitution. Furthermore, we find that the DOS at E_F can be increased by V or Cr substitution due to the distribution of d electrons near the E_F, which is in favor of enhancing the superconductivity. The 2D topological superconductivity from this nontrivial topological surface state might be induced by the superconductivity in the bulk as a result of the natural proximity effect between bulk and surface.

3.3. Discussion

In $NiTe_2$, the two Dirac points are located at $\mathbf{k} = (0, 0, \pm 0.35)(2\pi/c)$, which are distributed equally away from the Γ point along the [0 0 1] direction. Since the two bulk Dirac points project to the same point in the (0 0 1) surface, the surface Fermi loop only occurs on the side surfaces (i.e. parallel to the k_z axis). However, Fermi loop on DSM surface is not topologically protected [60], which is contrary to the robustly protected surface Fermi arcs in WSMs [6]. The Dirac points are much closer to the E_F in $NiTe_2$, unconventional odd-parity pairing states in connection with orbit-momentum locking as suggested in [28, 29] may occur in $NiTe_2$, although the rotational symmetry used to protect the type-II Dirac point (C_{3V} symmetry in $NiTe_2$) is different from D_{4h} crystal symmetry in [28, 29]. $NiTe_2$ belongs to type-II DSM, the Fermi surface contains both electron and hole pockets near the Dirac points, more carriers participate in pairing, but meantime suggesting a more complicated pairing scenario. Besides linear dispersion bands forming the tilted Dirac cone, there are trivial bands crossing the E_F as can be seen from the complicated Fermi surface discussed above, so we suggest that unconventional and conventional pairings coexist in $NiTe_2$ compound. For the isostructured $PdTe_2$ compound, the Dirac point is far away from the E_F, the superconducting phase in the bulk of $PdTe_2$ should be conventional in nature as pointed out in the experiments [37, 38]. For a topological Dirac superconductor, whether surface states composed of Majorana fermions appear depending on the pair potentials and surface direction [41]. For $NiTe_2$ compound, even if Majorana fermion related to the character of type-II DSM is present, it can only appear on the side surfaces (i.e. parallel to the k_z axis). This may not be easy to detect experimentally, since the natural cleavage plane of $NiTe_2$ family is the (0 0 1) surface (i.e. perpendicular to the k_z axis).

Fortunately, there is a nontrivial topological surface state on (0 0 1) surface, which is irrelevant to the type-II Dirac cone in the bulk, but originates from a nontrivial Z_2 invariant as discussed above. Our calculations show that a nontrivial topological surface state in $NiTe_2$ can be tuned to near the E_F by doping. For this helical surface state, it is very similar to that of

TI, its spin and momentum are locked and it is well separated from the bulk states. Fu and Kane explicitly demonstrated that Majorana zero modes can be realized in the surface states of a TI with proximity-induced s-wave pairing [61]. However, it is generally believed that the induced superconducting gap in the surface states is small due to high interfacial barrier and possible Fermi surface mismatch. While for $NiTe_2$ compound, this nontrival topological surface state is expected to be superconducting induced by the superconductivity in the bulk due to the natural proximity effect between bulk and surface. Unusual surface superconductivity observed in $PdTe_2$ compound [39, 40] has indicated indirectly this suggestion. So we speculate that 2D topological superconductivity is possible to be realized on the (0 0 1) surface of semimetal $NiTe_2$ compound.

4. Conclusions

In summary, our first-principles calculations show that $NiTe_2$ is a type-II DSM with Dirac cone titled along the [0 0 1] direction and the Dirac point is much closer to E_F. The phonon calculations show that the lattice dynamic is stable and the calculated Raman active modes as well as Debye temperature in our work are well consistent with the experimental values. Besides the vHs band near M point, it's particularly noteworthy that the nontrival bands around type-II Dirac point are strongly coupled with phonon modes, suggesting that they play an important role in superconductivity and provide various possibility of realizing topological superconductivity in $NiTe_2$. So we suggest that unconventional and conventional superconductivity coexist in $NiTe_2$ compound. Furthermore, the topological surface states on (0 0 1) surface originated from the nontrivial Z_2 invariant far away from the E_F can be tuned to approach the E_F by adding holes or by V substitution. By the natural proximity effect between bulk and surface, the 2D topological superconductivity from this nontrivial topological surface state might be induced by the superconductivity in the bulk. So we speculate that $NiTe_2$ is a promising material candidate for exploring topological superconductivity and it will therefore be of interest for further study.

Acknowledgments

This work is supported by the Natural Science Foundation from Jiangsu Province of China under Grant No. BK20141441.

ORCID iDs

G Q Huang https://orcid.org/0000-0002-1918-3113

References

[1] Scharf B *et al* 2019 Dynamical screening in monolayer transition-metal dichalcogenides and its manifestations in the exciton spectrum *J. Phys.: Condens. Matter* **31** 203001
[2] Kim K, Kim S, Kim J S, Kim H, Park J-H and Min B I 2018 Importance of the van Hove singularity in superconducting $PdTe_2$ *Phys. Rev.* B **97** 165102
[3] Soh J-R *et al* 2019 Ideal Weyl semimetal induced by magnetic exchange *Phys. Rev.* B **100** 201102
[4] Kozii V and Fu L 2015 Odd-parity superconductivity in the vicinity of inversion symmetry breaking in spin–orbit-coupled systems *Phys. Rev. Lett.* **115** 207002
[5] Wang Z, Weng H, Wu Q, Dai X and Fang Z 2013 Three-dimensional Dirac semimetal and quantum transport in Cd_3As_2 *Phys. Rev.* B **88** 125427
[6] Buckeridge J and Jevdokimovs D 2016 Nonstoichiometry and Weyl fermionic behavior in TaAs *Phys. Rev.* B **94** 180101
[7] Soluyanov A A, Gresch D, Wang Z, Wu Q, Troyer M, Dai X and Bernevig B A 2015 Type-II Weyl semimetals *Nature* **527** 495
[8] Sun Y, Wu S C, Ali M N, Felser C and Yan B 2015 Prediction of Weyl semimetal in orthorhombic $MoTe_2$ *Phys. Rev.* B **92** 161107
[9] Belopolski I *et al* 2016 Fermi arc electronic structure and Chern numbers in the type-II Weyl semimetal candidate $Mo_xW_{1-x}Te_2$ *Phys. Rev.* B **94** 085127
[10] Huang H, Zhou S and Duan W 2016 Type-II Dirac fermions in the $PtSe_2$ class of transition metal dichalcogenides *Phys. Rev.* B **94** 121117
[11] Zhang K, Yan M, Zhang H, Huang H, Arita M, Sun Z, Duan W, Wu Y and Zhou S 2017 Experimental evidence for type-II Dirac semimetal in $PtSe_2$ *Phys. Rev.* B **96** 125102
[12] Yan M *et al* 2017 Lorentz-violating type-II Dirac fermions in transition metal dichalcogenide $PtTe_2$ *Nat. Commun.* **8** 257
[13] Xiao R C *et al* 2017 Manipulation of type-I and type-II Dirac points in $PdTe_2$ superconductor by external pressure *Phys. Rev.* B **96** 075101
[14] Noh H J, Jeong J, Cho E J, Kim K, Min B I and Park B G 2017 Experimental realization of type-II Dirac fermions in a $PdTe_2$ superconductor *Phys. Rev. Lett.* **119** 016401
[15] Fei F *et al* 2017 Nontrivial Berry phase and type-II Dirac transport in the layered material $PdTe_2$ *Phys. Rev.* B **96** 041201
[16] Bahramy M S *et al* 2017 Ubiquitous formation of bulk Dirac cones and topological surface states from a single orbital manifold in transition-metal dichalcogenides *Nat. Mater.* **17** 21–8
[17] Xu C Q *et al* 2018 Topological Type-II Dirac Fermions approaching the Fermi levelz in a transition metal dichalcogenide $NiTe_2$ *Chem. Mater.* **30** 4823–30
[18] Armitage N P, Mele E J and Vishwanath A 2018 Weyl and Dirac semimetals in three dimensional solids *Rev. Mod. Phys.* **90** 15001
[19] Sato M and Ando Y 2017 Topological superconductors: a review *Rep. Prog. Phys.* **80** 076501
[20] Qi X L 2011 Topological insulators and superconductors *Rev. Mod. Phys.* **83** 1057
[21] Alicea J, Oreg Y, Refael G, von Oppen F and Fisher M P A 2011 Non-abelian statistics and topological quantum information processing in 1D wire networks *Nat. Phys.* **7** 412
[22] Alidoust M, Willatzen M and Jauho A P 2018 Strain-engineered Majorana zero energy modes and φ_0 Josephson state in black phosphorus *Phys. Rev.* B **98** 085414
[23] Qi Y *et al* 2016 Superconductivity in Weyl semimetal candidate $MoTe_2$ *Nat. Commun.* **7** 11038
[24] Chen F C *et al* 2016 Superconductivity enhancement in the S-doped Weyl semimetal candidate$MoTe_2$ *Appl. Phys. Lett.* **108** 162601
[25] Alidoust M, Willatzen M and Jauho A-P 2018 Fraunhofer response and supercurrent spin switching in black phosphorus with strain and disorder *Phys. Rev.* B **98** 184505

[26] Heikes C *et al* 2018 Mechanical control of crystal symmetry and superconductivity in Weyl semimetal $MoTe_2$, *Phys. Rev. Mater.* **2** 074202
[27] Wei H, Chao S and Aji V 2014 Odd-parity superconductivity in Weyl semimetals *Phys. Rev.* B **89** 014506
[28] Hashimoto T, Kobayashi S, Tanaka Y and Sato M 2016 Superconductivity in doped Dirac semimetals *Phys. Rev.* B **89** 014510
[29] Kobayashi S and Sato M 2015 Topological superconductivity in Dirac semimetals *Phys. Rev. Lett.* **115** 187001
[30] Alidoust M, Willatzen M and Jauho A-P 2019 Control of superconducting pairing symmetries in monolayer black phosphorus *Phys. Rev.* B **99** 125417
[31] Alidoust M, Halterman K and Zyuzin A A 2017 Superconductivity in type-II Weyl semimetals *Phys. Rev.* B **95** 155124
[32] Li D, Rosenstein B, Shapiro B Y and Shapiro I 2017 Effect of the type I to type II Weyl semimetal topological transition on superconductivity *Phys. Rev.* B **95** 094513
[33] Jellinek F 1963 Sulfides of the transition metals of groups IV, V and VI *Arkiv Kemi* **20** 447
[34] Raub Ch J *et al* 1965 The phase diagram of KNO_3 to 40 kbars *J. Phys. Chem. Solids* **26** 12
[35] Liu Y *et al* 2015 Electronic structure of transition metal dichalcogenides $PdTe_2$ and $Cu_{0.05}PdTe_2$ superconductors obtained by angle-resolved photoemission spectroscopy *Chin. Phys.* B **24** 067401
[36] Kudo K, Ishii H and Nohara M 2016 Composition-induced structural instability and strong-coupling superconductivity in $Au_{1-x}Pd_xTe_2$ *Phys. Rev.* B **93** 140505
[37] Das S, Amit V, Sirohi A, Yadav L, Gayen S, Singh Y and Sheet G 2018 Conventional superconductivity in the type-II Dirac semimetal $PdTe_2$ *Phys. Rev.* B **97** 014523
[38] Amit V and Singh Y 2018 Heat capacity evidence for conventional superconductivity in the type-II Dirac semimetal $PdTe_2$ *Phys. Rev.* B **97** 054515
[39] Leng H, Paulsen C, Huang Y K and de Visser A 2017 Type-I superconductivity in the Dirac semimetal $PdTe_2$ *Phys. Rev.* B **96** 220506
[40] Leng H *et al* 2020 Superconductivity under pressure in the Dirac semimetal $PdTe_2$ *J. Phys.: Condens. Matter* **32** 025603
[41] Lima B S *et al* 2018 Properties and superconductivity in Ti-doped $NiTe_2$ single crystals *Solid State Commun.* **283** 27–31
[42] Santos F B, Correa L E, Renosto S T, Lima B S, Jardim R F, Torikachvili M and Machado A J S 2014 Superconductivity in $NiTe_2$ compounds interspersed with layers of Ti and Cu *APS March Meeting* vol 59 (https://meetings.aps.org/Meeting/MAR14/Session/C1.100)
[43] Le T, Yin L, Feng Z, Huang Q, Che L, Li J, Shi Y and Lu X 2019 Single full gap with mixed type-I and type-II superconductivity on surface of the type-II Dirac semimetal $PdTe_2$ by point-contact spectroscopy *Phys. Rev.* B **99** 180504
[44] Clark O J *et al* 2018 Fermiology and superconductivity of topological surface states in $PdTe_2$ *Phys. Rev. Lett.* **120** 156401
[45] Liu Y *et al* 2015 Identification of topological surface state in $PdTe_2$ superconductor by angle-resolved photoemission spectroscopy *Chin. Phys. Lett.* **32** 067303
[46] Betancourt J, Li S, Dang X, Burton J D, Tsymbal E Y and Velev J P 2016 Complex band structure of topological insulator Bi_2Se_3 *J. Phys.: Condens. Matter* **28** 395501
[47] Hao L and Wang J 2015 Superconductivity in the surface states of a Bi_2Se_3 topological insulator: effects of a realistic model *J. Phys.: Condens. Matter* **27** 255701
[48] Giannozzi P *et al* 2009 QUANTUM ESPRESSO: a modular and open-source software project for quantum simulations of materials *J. Phys.: Condens. Matter* **21** 395502
[49] Li T and Galli G 2007 Electronic properties of MoS_2 nanoparticles *J. Phys. Chem.* C **111** 16192
[50] Marzari N *et al* 2012 Maximally localized Wannier functions: theory and applications *Rev. Mod. Phys.* **84** 1419
[51] Wu Q S *et al* 2018 WannierTools: an open-source software package for novel topological materials *Comput. Phys. Commun.* **224** 405–16
[52] Poncé S, Margine E R, Verdi C and Giustino F 2016 EPW: electron–phonon coupling, transport and superconducting properties using maximally localized Wannier functions *Comput. Phys. Commun.* **209** 116–33
[53] Yang E, Ji H and Jung Y 2015 Two-dimensional transition metal dichalcogenide monolayers as promising sodium ion battery anodes *J. Phys. Chem.* C **119** 26374–80
[54] Tchoumakov S, Civelli M and Goerbig M O 2016 Magnetic-field-induced relativistic properties in type-I and type-II Weyl semimetals *Phys. Rev. Lett.* **117** 086402
[55] Grimvall G 1981 The electron–phonon interaction in metals *Selected Topics in Solid State Physics* ed E Wohlfarth (Amsterdam: North-Holland)
[56] Giustino F, Cohen L M and Louie S G 2007 Electron–phonon interaction using Wannier functions *Phys. Rev.* B **76** 165108
[57] Allen P B and Dynes R C 1975 Transition temperature of strong-coupled superconductors reanalyzed *Phys. Rev.* B **12** 905
[58] Annese E *et al* 2016 Nonvortical Rashba spin structure on a surface with C_{1h} symmetry *Phys. Rev. Lett.* **117** 016803
[59] Ren X L *et al* 2019 Gate-tuned insulator-metal transition in electrolyte-gated transistors based on tellurene *Nano Lett.* **19** 4738–44
[60] Kargariana M, Randeriaa M and Lu Y M 2016 Are the surface Fermi arcs in Dirac semimetals topologically protected? *Proc. Natl Acad. Sci.* **113** 8648–52
[61] Fu L and Kane C L 2008 Superconducting proximity effect and Majorana fermions at the surface of a topological insulator *Phys. Rev. Lett.* **100** 096407